

Cite this: *Dalton Trans.*, 2018, **47**,
15957

Low thermal conductivity and high figure of merit for rapidly synthesized n-type $\text{Pb}_{1-x}\text{Bi}_x\text{Te}$ alloys†

Tingting Chen,^a Hongchao Wang,^a *^{a,b} Wenbin Su,^a Fahad Mehmood,^a
Teng Wang,^a Jinze Zhai,^a Xue Wang^a and Chunlei Wang*^a

High figures of merit of n-type $\text{Pb}_{1-x}\text{Bi}_x\text{Te}$ alloys have been achieved by rapid synthesis at low temperature. The effects of Bi dopant and microwave hydrothermal technology on microstructure and thermoelectric performance have been studied. The solid solubility limit of Bi in PbTe is between $x = 0.02$ and 0.03 . Homogenous nanopowders of about 70 nm have been synthesized by the microwave hydrothermal method. When followed by hot pressing, sub-microscale grain sizes are also formed for $\text{Pb}_{1-x}\text{Bi}_x\text{Te}$ alloys. With increase in Bi, the carrier concentration is improved within the solubility limit. This leads to low electrical resistivity and higher power factor at high temperature. A higher power factor of $8.5 \mu\text{W cm}^{-1} \text{K}^{-2}$ is obtained for $x = 0.02$ sample at 623 K. In addition, the introduction of Bi effectively prohibits the p–n transition and bipolar thermal conductivity of pristine PbTe. Thus, a low lattice thermal conductivity of $0.68 \text{ W m}^{-1} \text{K}^{-1}$ is achieved at 673 K, combining scattering of alloys, grain boundaries, dislocations and defects. As a result, the highest peak figure of merit, *i.e.*, $zT = 0.62$ at 673 K is achieved for $\text{Pb}_{0.98}\text{Bi}_{0.02}\text{Te}$ sample, which is comparable with that of Bi-doped PbTe alloys synthesized by the conventional melting method. Thus, the right synthesis conditions of the microwave hydrothermal method can rapidly result in thermoelectric materials with comparable figures of merit.

Received 19th August 2018,
Accepted 16th October 2018

DOI: 10.1039/c8dt03387k

rsc.li/dalton

Introduction

Thermoelectric materials can directly convert heat into electricity and *vice versa* and play an increasingly important role in sustainable energy.^{1–3} The performance of thermoelectric materials is determined by the dimensionless figure of merit $zT = S^2T/[\rho(\kappa_e + \kappa_L)]$, where T , S , ρ , κ_e , and κ_L are the absolute temperature, Seebeck coefficient, electrical resistivity, and electronic and lattice thermal conductivities, respectively.^{4–6} The total thermal conductivity (κ_{tot}) is the sum of electronic (κ_e) and lattice (κ_L) contributions. Thus, a high-performance thermoelectric material should have a high Seebeck coefficient, low electrical resistivity and low thermal conductivity. These parameters are strongly dependent on the carrier concentration (n) and hence, optimized carrier concentrations are needed.^{7–9} In addition, nanostructures are generally used to reduce lattice thermal conductivity.^{10–13} Therefore, enhance-

ment in figure of merit can be achieved by optimizing carrier concentration and modifying nanostructures.

Lead telluride (PbTe) is a typical middle-temperature (500–900 K) thermoelectric material, which has promising applications in recycling waste heat from factories and engines. As we know, the figures of merit for p-type PbTe alloys have significantly improved in recent years. Some higher figures of merit, which are over the desired threshold value of 2.0, have been reported recently.^{11,14–19} To achieve high conversion efficiency for thermoelectric modules, higher figures of merit for both p- and n-type materials are required. Unfortunately, the current zT values of n-type PbTe alloys are relatively lower compared with those of p-type materials. It is observed that band structure engineering does not effectively enhance the Seebeck coefficient of n-type PbTe. In addition, the thermal conductivity is higher and bipolar thermal conductivity is not prohibited. Therefore, optimization of carrier concentration, nanostructure, point defects, *etc.* is generally applied to modify the thermoelectric performances of n-type PbTe alloys. Aaron D. Lalonde *et al.* reported the effect of carrier concentration modification on thermoelectric performances for n-type $\text{PbTe}_{1-x}\text{I}_x$ alloys prepared by melting at 1273 K for 6 h and annealing at 973 K for 48 h, followed by hot pressing.⁹ As a result, a high zT value of 1.4 was obtained between 700 and 850 K by precise control of the doping level. Combining low lattice thermal conductivity by Ag_2Te nanopre-

^aSchool of Physics, State Key Laboratory of Crystal Materials, Shandong University, Jinan 250100, China. E-mail: wanghc@sdu.edu.cn, wangcl@sdu.edu.cn

^bState Key Laboratory of Metastable Materials Science and Technology, Yanshan University, Qinhuangdao 066000, China

† Electronic supplementary information (ESI) available: Distribution of grain, EDS mapping, Lorenz numbers, heat capacities, thermal diffusivities, electronic thermal conductivities, repeated measurements, densities and atom percentage of each element for $\text{Pb}_{1-x}\text{Bi}_x\text{Te}$ samples. See DOI: 10.1039/c8dt03387k

cipitates and optimized carrier concentration through La doping, the higher figure of merit $zT > 1.5$ has been achieved at 775 K for La-doped $(\text{PbTe})_{1-x}(\text{Ag}_2\text{Te})_x$ alloys synthesized by the conventional solid state reaction.²⁰ The electrical and thermal properties have been modified by Sb and S incorporation and a higher figure of merit, $zT = 1.4$ at 900 K, has been obtained for n-type PbTe alloys.²¹ Their samples were synthesized by melting at 1373 K for 6 h and annealing at 873 K for 12 h, followed by spark plasma sintering (SPS). Recently, a state-of-the-art thermoelectric figure of merit of about 1.8 was achieved for two n-type PbTe compositions obtained by melting, ball milling and SPS.^{22,23} One is the incorporation of InSb into the PbTe matrix, resulting in multiphase nanostructures; this can simultaneously optimize both electrical and thermal transport, leading to excellent thermoelectric performances.²² The other contains dual-site substitutional point defects formed by Sb doped in $\text{PbTe}_{0.998}\text{I}_{0.002}$ composition;²³ in this case, the dual-site point defects improve the figure of merit by simultaneously modifying power factor and lattice thermal conductivity. In the above-mentioned observations, the thermoelectric performances have certainly been improved. Meanwhile, it is clearly found that these reported n-type PbTe alloys with excellent properties are always synthesized by the conventional melting method, requiring high melting temperatures and long times.

In recent years, the microwave hydrothermal method has become a popular chemical synthesis method, which combines the advantages of microwave heating and hydrothermal methods. It can decrease the experimental temperature, shorten the reaction time, and improve the experimental efficiency. In addition, obtained powders show high purity, good crystallinity and uniform microstructures.^{24–26} Few thermoelectric materials have been prepared in this way, and the corresponding properties are also reported. For instance, pristine SnTe alloys have been successfully synthesized by the microwave hydrothermal method followed by SPS.²⁵ In this process, the reaction temperature and time are 220 °C and 20 min, respectively. The high figure of merit 0.49 was achieved for SnTe alloy with optimized reaction conditions, and it is comparable to that of the conventional melting method. Therefore, microwave hydrothermal synthesis can be used to prepare n-type PbTe-based alloys, and high figures of merit can be obtained with the right synthesis conditions using this method.

From the above reported study, we infer that Sb is one of the best doping elements to optimize thermoelectric performances for n-type PbTe alloys.^{21,23} Bi has the same configuration as that of Sb, and it is also a good selection as an n-type dopant of PbTe alloys for thermoelectric performance modification. In this study, Bi-doped PbTe compositions have been chosen and synthesized by the microwave hydrothermal method followed by hot pressing. Within the solid solubility limit of Bi, the carrier concentrations and electrical properties have been tuned and then, the power factor is enhanced with Bi doping at high temperature. A higher power factor of $8.5 \mu\text{W cm}^{-1} \text{K}^{-2}$ has been obtained for $x = 0.02$ sample at

623 K. In addition, the lattice thermal conductivity shows a decreasing trend, and a lower lattice thermal conductivity of about $0.68 \text{ W m}^{-1} \text{K}^{-1}$ is obtained at 673 K. In total, the higher figure of merit 0.62 has been achieved at 673 K for $\text{Pb}_{0.98}\text{Bi}_{0.02}\text{Te}$ alloy; this value is comparable with that of the material synthesized by the conventional melting method.

Experimental

$\text{Pb}_{1-x}\text{Bi}_x\text{Te}$ ($x = 0.00, 0.01, 0.02, 0.03$ and 0.04) alloys were synthesized by the microwave hydrothermal method followed by hot pressing. Lead nitrate (PbN_2O_6 , 99.99%), sodium tellurite (Na_2TeO_3 , 97%), bismuth chloride (BiCl_3 , 99%), sodium hydroxide (NaOH , 96%) and sodium borohydride (NaBH_4 , 98%) were purchased from Shanghai Aladdin Biochemical Technology Co., Ltd and used as precursors without any further purification.

In a typical synthesis of PbTe nanopowders, 2 g of NaOH, 1.9788 g PbN_2O_6 , 1.3646 g Na_2TeO_3 and 0.6 g NaBH_4 were successively added to 50 mL deionized water (proportionate BiCl_3 was added for Bi-doped PbTe samples with decreasing quantity of PbN_2O_6). The solution was transferred to an 80 mL Teflon autoclave and was heated to 140 °C for 30 min at the heating rate of 10 °C min^{-1} in the microwave hydrothermal synthesizer (XH-800S, Beijing XiangHu Science and Technology Development Co., Ltd, China). The products were cooled to room temperature naturally and then centrifuged and washed several times with deionized water and ethanol. After that, these washed products were dried to powder in a vacuum oven. The obtained PbTe nanopowders were sintered by hot pressing at 773 K for 1 h under 20 MPa. Finally, $\text{Pb}_{1-x}\text{Bi}_x\text{Te}$ samples with high relative densities >97% were synthesized.

The phase structures of all samples were investigated by X-ray diffraction (XRD, D8 ADVANCE) using Cu K-alpha radiation. To probe the optical energy band gaps of the samples, room temperature optical diffuse reflectance measurements were performed using a Nicolet 6700 FTIR spectrometer in the frequency range of $4000\text{--}400 \text{ cm}^{-1}$ with 4 cm^{-1} resolution. The microstructure and chemical composition of the samples were analyzed by transmission electron microscopy (TEM, JEM-2010 and FEI Tecnai F20) and field emission scanning electron microscopy (SEM, JSM-7610F) with energy dispersive spectrometry (EDS). The TEM samples were prepared by focused ion beam (FIB). X-ray photoelectron spectra (XPS, ESCALAB 250) were performed using Al K α X-rays (1261 eV). The room-temperature Hall coefficient (R_{H}) of the samples was measured on a home-made system under a reversible magnetic field of 0.6 T and an electrical current of 100 mA. The carrier concentration (n) of each sample was estimated by the relationship $n = 1/eR_{\text{H}}$, where e is the electronic charge. The Hall mobility (μ_{H}) was calculated using the equation $\mu_{\text{H}} = 1/\rho R_{\text{H}}$. The electrical resistivity and Seebeck coefficient were simultaneously measured under a He atmosphere from 323 K to 673 K using an LSR-3 instrument. The thermal diffusivity (λ) was measured with a laser thermal conductivity instrument (LFA-457). The

heat capacity (C_p) was estimated with the equation of C_p (k_B atom) = $3.07 + 4.7 \times 10^{-4} \times (T/K - 300)$,²⁷ as shown in Fig. S4(a).† Total thermal conductivity (κ_{tot}) was calculated with the equation $\kappa_{\text{tot}} = \lambda C_p d$, in which the density (d) was measured using the Archimedes' method. The figures of merit were obtained based on above-mentioned parameters.

Results and discussion

Fig. 1(a) shows the XRD patterns of $\text{Pb}_{1-x}\text{Bi}_x\text{Te}$ nanopowders at room temperature synthesized by the microwave hydrothermal method. All the diffraction peaks can be indexed to face-centered cubic PbTe with space group $Fm\bar{3}m$ (225) (PDF#65-0881). No impurity diffraction peaks were found in XRD patterns for any powder. Thus, $\text{Pb}_{1-x}\text{Bi}_x\text{Te}$ nanopowders with single phase structure were successfully prepared. The XRD patterns for $\text{Pb}_{1-x}\text{Bi}_x\text{Te}$ bulk alloys are shown in Fig. 1(b). These alloys are obtained by hot pressing sintering of achieved nanopowders. It is clear that the XRD patterns for alloys are identical with those of corresponding powders. All alloy samples show a pure single phase of cubic crystal structure. Thus, the process of hot pressing does not affect the crystal structure, and $\text{Pb}_{1-x}\text{Bi}_x\text{Te}$ alloys with single cubic phase have been synthesized. Based on the XRD data of $\text{Pb}_{1-x}\text{Bi}_x\text{Te}$ alloys, the lattice constants as a function of dopant concentration (x) of alloy samples were calculated and are presented in Fig. 1(c). The lattice constant of pristine PbTe is 6.464 Å, which is in agreement with the previously reported value.²⁸ With Bi doping, the lattice constant decreases with increasing dopant concentration up to $x = 0.02$ and remains almost the same when x is further increased. Since the radius of Bi^{3+} (1.08 Å) is much smaller than that of Pb^{2+} (1.20 Å), decrease in lattice constant is found. The turning point of lattice constant vs. doping concentration is observed at $x = 0.02$, as shown in Fig. 1(c). In addition, the chemical compositions of $\text{Pb}_{1-x}\text{Bi}_x\text{Te}$ nanopowders were analyzed by EDS mapping, as shown in Table S2.† The content of Bi increases until $x = 0.03$ although the EDS measurement contains certain error because of the limit of EDS mapping. Considering lattice constants and element analysis, the solid solubility limit of Bi in PbTe should be between $x = 0.02$ and 0.03. This inference of solid solubility limit is consistent with the following microstructural and physical properties; however, it is seemingly contradictory with XRD patterns for samples with more Bi doping. This may result from the microwave hydrothermal method. The over-dopants are dissolved in liquid and can be washed away in the end. Thus, the impurity phases are not found for over-doped samples. In summary, $\text{Pb}_{1-x}\text{Bi}_x\text{Te}$ alloys with a single cubic phase have been formed by the microwave hydrothermal method followed by hot pressing.

The direct band gaps for all samples have been studied. These values are derived from the measurement of optical absorption, as shown in Fig. 2. The values of direct band gaps can result from the intercept on the energy axis according to the relationship $\alpha = \alpha_0[(E - E_g)/E_g]^n$, where α , α_0 , E , E_g , C and n

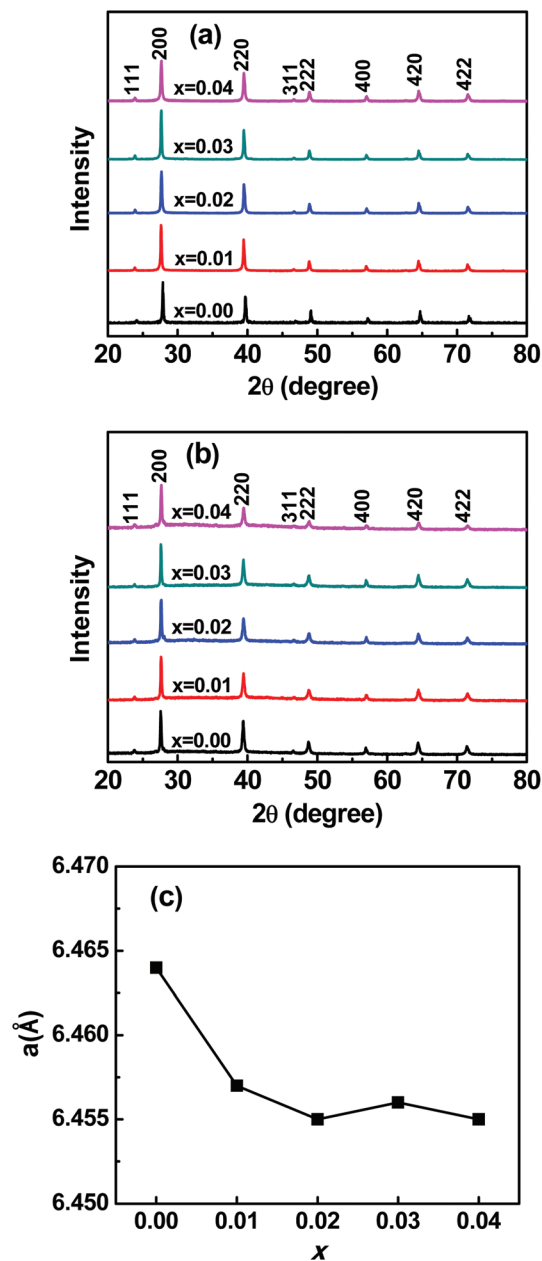


Fig. 1 XRD patterns at room temperature of (a) nanopowders and (b) bulk alloys for $\text{Pb}_{1-x}\text{Bi}_x\text{Te}$ compositions. (c) Lattice constants of $\text{Pb}_{1-x}\text{Bi}_x\text{Te}$ bulk alloys.

are the absorption coefficient, a constant, energy, band gap, instrumental shift, and 1/2 for a direct band gap, respectively. In Fig. 2, the band gap value of 0.28 eV has been obtained for pristine PbTe alloy, which is consistent with a previously reported value.¹⁹ With Bi doping, the direct band gaps do not change clearly; the values of direct band gaps are very near to that of pristine sample. In other words, Bi as a dopant does not clearly affect the direct band gap of PbTe.

The morphologies and microstructures of $\text{Pb}_{1-x}\text{Bi}_x\text{Te}$ nanopowders were scanned, and all SEM images are displayed in Fig. 3(a–e). In general, the morphology of all nanopowders is

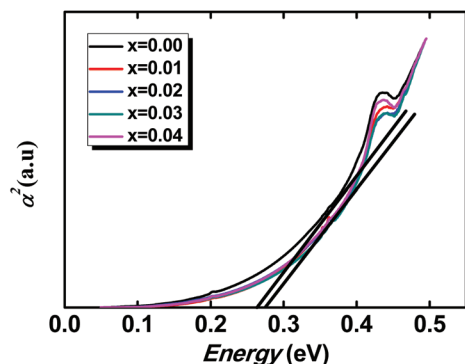


Fig. 2 The optical absorption spectra replotted as α^2 vs. energy for $\text{Pb}_{1-x}\text{Bi}_x\text{Te}$ bulk alloys.

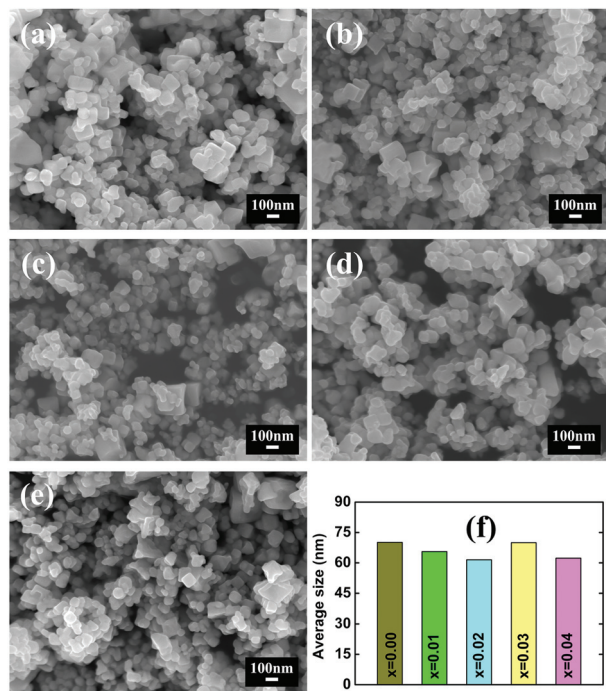


Fig. 3 SEM images of $\text{Pb}_{1-x}\text{Bi}_x\text{Te}$ nanopowders for (a) $x = 0.00$, (b) $x = 0.01$, (c) $x = 0.02$, (d) $x = 0.03$, and (e) $x = 0.04$. (f) Average grain size of $\text{Pb}_{1-x}\text{Bi}_x\text{Te}$ nanopowders.

cubic. In addition, the grain size distribution for each nanopowder is relatively uniform and most grain sizes are in the 40–100 nm range, as shown in Fig. S1.† The average grain size for each nanopowder is presented in Fig. 3(f). It is shown that the average grain size of all nanopowders is about 70 nm. Thus, $\text{Pb}_{1-x}\text{Bi}_x\text{Te}$ nanopowders with relatively better crystal shape and uniform size have been rapidly prepared by the microwave hydrothermal method. Fig. 4(a–e) show the cross-sectional SEM images for $\text{Pb}_{1-x}\text{Bi}_x\text{Te}$ bulk alloys. It is easily found that the grain sizes for all samples are evidently enlarged compared with that of the nanopowders. The average grain sizes are between 0.9 μm and 2.6 μm for all samples, as shown in Fig. 4(f), which are much larger than that of nano-

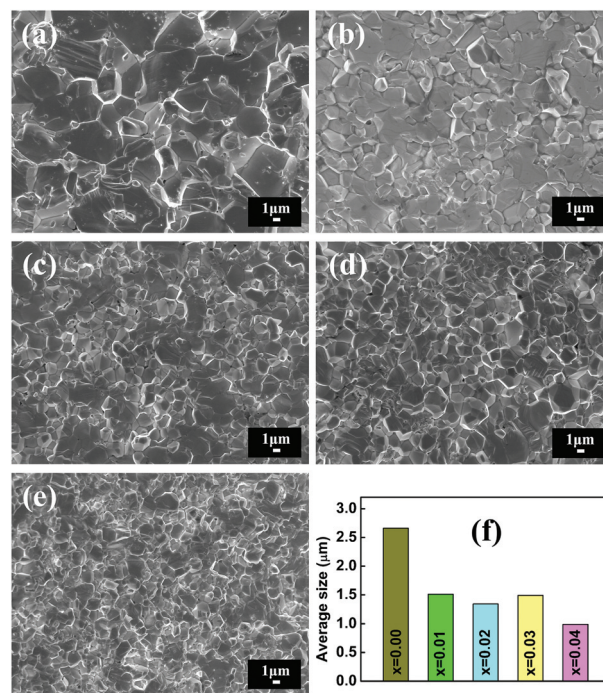


Fig. 4 SEM images of $\text{Pb}_{1-x}\text{Bi}_x\text{Te}$ bulk alloys for (a) $x = 0.00$, (b) $x = 0.01$, (c) $x = 0.02$, (d) $x = 0.03$, and (e) $x = 0.04$. (f) Average grain size of $\text{Pb}_{1-x}\text{Bi}_x\text{Te}$ bulk alloys.

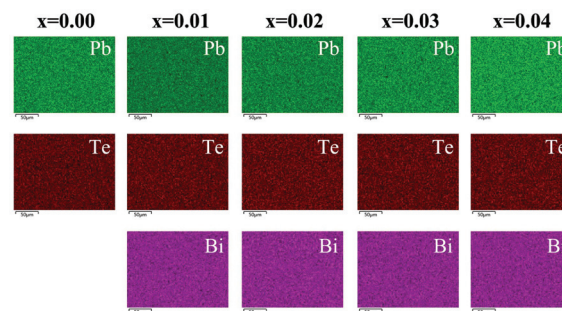


Fig. 5 EDS mapping of polished surface for $\text{Pb}_{1-x}\text{Bi}_x\text{Te}$ bulk alloys.

powders (70 nm). This phenomenon further confirms that grains can be grown with high-temperature sintering process. It is also observed that the average grain size decreases with Bi doping, which indicates that Bi can prohibit the grain growth in hot-pressing process. Additionally, the grain size distributions are counted and displayed in Fig. S2.† Although the average grain size is below 2.6 μm for all samples, a number of nano-grains with grain size less than 500 nm and large micro-grains of over 3 μm are also present in each sample, as shown in Fig. S2.† Therefore, it can be concluded that various-scaled grains have been formed, which is helpful in reducing the thermal conductivity. In addition to morphology and grain size from SEM images, EDS mappings are also conducted for element distributions. Fig. 5 shows the EDS mapping of polished surface for $\text{Pb}_{1-x}\text{Bi}_x\text{Te}$ bulk alloys. It can be found

that the elements are not abundant in all alloys; Pb, Te and Bi are homogeneously distributed. Since the excess Bi dopant over the solid solubility limit has been washed away, the $x = 0.03$ and 0.04 samples also show homogenous element distribution. In the end, $\text{Pb}_{1-x}\text{Bi}_x\text{Te}$ alloys with compact microstructure and homogenous element distributions have been successfully synthesized.

In addition to SEM images and element distributions, low magnification high angle annular dark field images (HAADF) and high resolution TEM images (HRTEM) for pristine PbTe and $\text{Pb}_{0.98}\text{Bi}_{0.02}\text{Te}$ alloys are shown in Fig. 6. It is clearly seen that dislocations are found in both samples. For pristine PbTe, the dislocations are numerous in grain boundaries and form a dislocation network. For $\text{Pb}_{0.98}\text{Bi}_{0.02}\text{Te}$ alloy, most dislocations are in grains with high densities and few are in grain boundaries. Thus, with the introduction of Bi, most dislocations transfer from grain boundaries to inside grains. In the HAADF images, although some defects are found, they are also found to exhibit single crystal phase from the selected area electron diffraction pattern (SAED); no other diffraction spots emerge. These defects and dislocations are beneficial for reducing lattice thermal conductivity, as shown in the following descriptions.

Fig. 7 presents the XPS survey spectrum of $\text{Pb}_{0.98}\text{Bi}_{0.02}\text{Te}$ alloy and high resolution XPS spectrum of Bi 4f. All peaks can be assigned to Pb, Te, Bi, O and C, as shown in Fig. 7(a). The Bi 4f_{5/2} and Bi 4f_{7/2} peaks were observed at about 163 and 157 eV, respectively, as shown in Fig. 7(b), which are consistent with previously reported results.^{29,30} With these results, the valence state of Bi³⁺ is confirmed. Thus, when Bi³⁺ is substi-

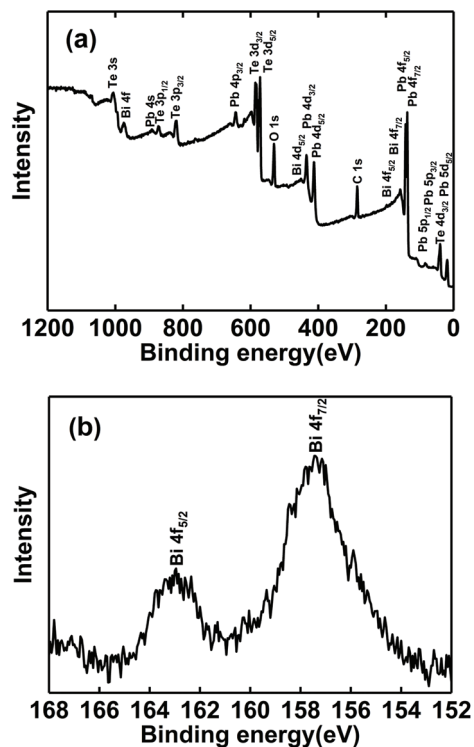


Fig. 7 (a) XPS survey spectrum of $\text{Pb}_{0.98}\text{Bi}_{0.02}\text{Te}$ alloy. (b) High resolution XPS spectrum of Bi 4f of $\text{Pb}_{0.98}\text{Bi}_{0.02}\text{Te}$ alloy.

tuted at the site of Pb^{2+} , more electrons are formed. Bi is an n-type dopant for PbTe, just as the initial proposal.

The results for electrical resistivities of $\text{Pb}_{1-x}\text{Bi}_x\text{Te}$ alloys are shown in Fig. 8(a). For pristine PbTe, shown in the inserted figure, the electrical resistivity increases with increasing temperature up to ~ 500 K and then decreases with further increase in temperature. In other words, it shows a metal-semiconductor transition around 500 K. This transitional behavior is consistent with previously reported results; the only difference is that the transitional temperature is slightly different from previously reported results.^{28,31,32} With the Bi doping, the electrical resistivity behavior changes to semiconductor-metal transition. With increasing Bi content, the transitional temperature moves toward a higher temperature range, *i.e.*, from 426 K to 527 K. For semi-conductive behavior at a relatively low temperature, the grain boundaries, dislocations and defects found in SEM and TEM images are predominantly scattering the carriers. These localized factors lead to semi-conductive behavior.³³ Within the measured temperature limit, the lowest electrical resistivity of about $4.5 \text{ m}\Omega \text{ cm}$ has been obtained at a transitional temperature for $x = 0.02$ and 0.03 alloys. In the temperature range of metallic conduction behavior, the electrical resistivity reduces and then slightly increases with increasing Bi content. This behavior is relative to the solid solubility limit between $x = 0.02$ and 0.03 , as in the above description. In the semi-conductivity range, no clear trend is observed. To understand the electrical resistivity at room temperature, carrier concentration and mobility are

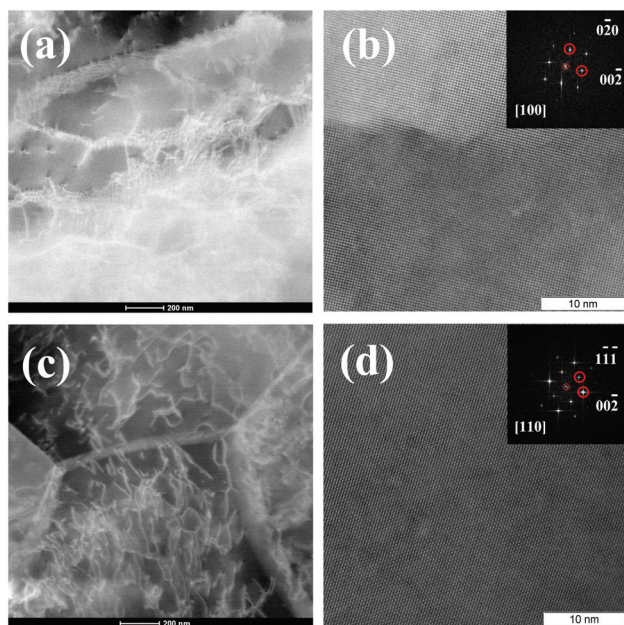


Fig. 6 (a) HAADF image and (b) HRTEM image with inserted SAED pattern for pristine PbTe sample; (c) HAADF image and (d) HRTEM image with inserted SAED pattern for $\text{Pb}_{0.98}\text{Bi}_{0.02}\text{Te}$ sample.

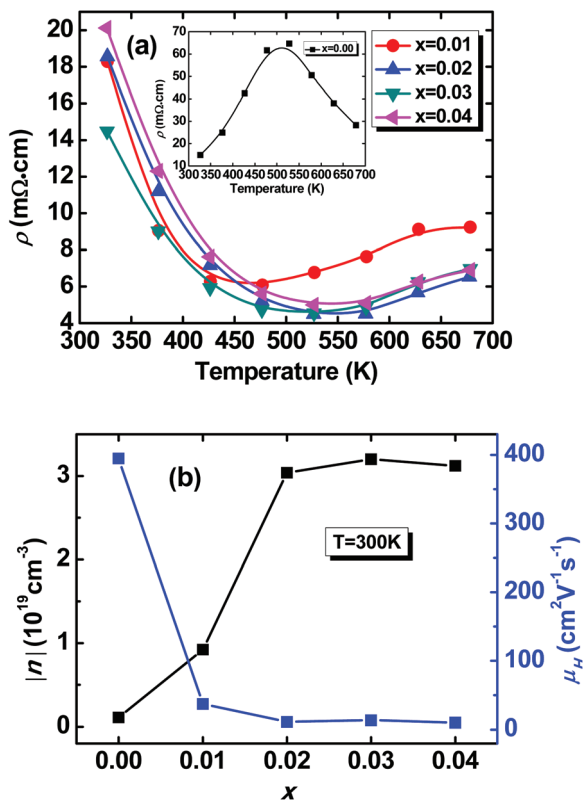


Fig. 8 (a) The temperature dependence of electrical resistivity for $\text{Pb}_{1-x}\text{Bi}_x\text{Te}$ alloys. (b) The absolute value of carrier concentration and mobility at room temperature.

presented in Fig. 8(b). The carrier concentration is positive for pristine PbTe, which indicates that it is a p-type semiconductor at room temperature. With Bi doping, all carrier concentrations change to negative values, which demonstrates that the main carriers are electrons for Bi-doped PbTe alloys. This results from Bi^{3+} substitution on the site of Pb^{2+} , which is confirmed by XPS spectra, as shown in Fig. 7. The carrier concentration for pure PbTe alloy is $0.1 \times 10^{19} \text{ cm}^{-3}$, which is consistent with previously reported values.²⁸ The absolute value of carrier concentration is significantly enhanced with increasing Bi content up to $x = 0.02$ and then increases slightly from $x = 0.02$ to 0.03. This further confirms that the solid solubility limit of Bi in PbTe alloy is in between $x = 0.02$ and 0.03. The electron mobility is extremely small for Bi-doped PbTe alloys compared with high hole mobility of $394 \text{ cm}^2 \text{ V}^{-1} \text{ s}^{-1}$ for pristine PbTe alloy; this results from Bi substitution on Pb site and small grain sizes. Thus, the lower electrical resistivities for $x = 0.02$ and 0.03 samples are mainly due to higher carrier concentrations.

Fig. 9(a) shows the temperature dependence of the Seebeck coefficient for $\text{Pb}_{1-x}\text{Bi}_x\text{Te}$ alloys. The value of Seebeck coefficient changes from positive to negative for pristine PbTe alloy at the temperature of $\sim 550 \text{ K}$, as shown in the inset of Fig. 9(a). This indicates that the main charge carriers are transferred from holes to electrons in the measured temperature

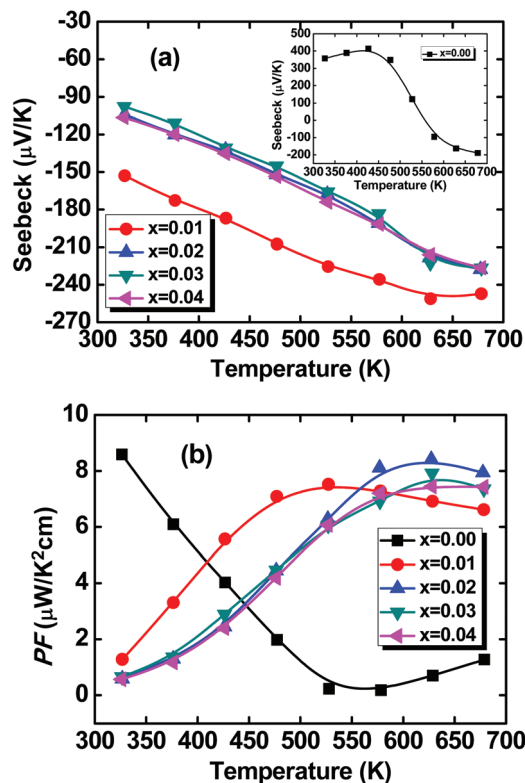


Fig. 9 The temperature dependence of (a) Seebeck coefficient and (b) power factor for $\text{Pb}_{1-x}\text{Bi}_x\text{Te}$ alloys.

range. The transitional temperature of 550 K is in the temperature range of semiconductor–metal transition for electrical resistivity. With Bi doping, the values of Seebeck coefficients of all samples become negative in the entire temperature range, which indicates that electrons are the main charge carriers and Bi is an n-type dopant for PbTe compositions. This is in good agreement with negative values of carrier concentrations at room temperature presented in Fig. 8(b). As the Bi-doped PbTe alloys are typical degenerate semiconductors with higher electrical concentrations over 10^{19} cm^{-3} , the absolute Seebeck coefficients increase with increasing temperature over the entire measured temperature range, as shown in Fig. 9(a). The absolute Seebeck coefficients decrease with increasing Bi content up to $x = 0.03$ and increase slightly for $x = 0.04$. This is because the Seebeck coefficient is inversely proportional to carrier concentration. As shown in Fig. 8(b), the $x = 0.03$ sample shows the highest carrier concentration; thus, its absolute Seebeck coefficient has the lowest value, as shown in Fig. 9(a). In this case, the $x = 0.01$ sample has the largest absolute Seebeck coefficient value in the whole measured temperature range. The absolute values of Seebeck coefficients are $153 \mu\text{W cm}^{-1} \text{ K}^{-2}$ and $251 \mu\text{W cm}^{-1} \text{ K}^{-2}$ at room and high temperatures, respectively, for $\text{Pb}_{0.99}\text{Bi}_{0.01}\text{Te}$ alloy.

The power factors (PF), calculated according to the formula of $PF = S^2/\rho$, are plotted in Fig. 9(b). The power factor decreases with increase in temperature until 528 K and then increases up to the measured limit for pristine PbTe alloy. This turning

point of power factor is almost the same as the transitional temperature of electrical resistivity and Seebeck coefficient. The highest value for power factor of about $8.5 \mu\text{W cm}^{-1} \text{K}^{-2}$ is observed at 326 K for pure PbTe alloy. The behaviors of temperature dependence of power factors change with Bi doping. The power factor first increases and then slightly decreases with increasing temperature for all Bi-doped samples. Thus, the peak values of power factors shift to a higher temperature range. In other words, the power factor is enhanced at middle and high temperature ranges with Bi doping. The maximum value of power factor reaches about $8.5 \mu\text{W cm}^{-1} \text{K}^{-2}$ at 623 K for $x = 0.02$. This results from the lowest electrical resistivity and moderate Seebeck coefficient at high temperature range.

The total thermal conductivities for $\text{Pb}_{1-x}\text{Bi}_x\text{Te}$ alloys are displayed in Fig. 10(a). With increasing temperature, the total thermal conductivity decreases, especially for the Bi-doped sample. The lowest total thermal conductivity of $0.85 \text{ W m}^{-1} \text{K}^{-1}$ is obtained at 673 K. The total thermal conductivities of Bi-doped samples do not show a clear trend at a low temperature in comparison with that of pristine sample, whereas the value of total thermal conductivity over 472 K is significantly lower. The lattice thermal conductivity is calculated and presented in Fig. 10(b), which is obtained by subtracting electronic thermal conductivity from total thermal conductivity. Here, the electronic thermal conductivity is calculated by the formula $\kappa_e = LT/\rho$, where L is the Lorenz number and is derived

from the equation $L = 1.5 + \exp(-|S|/116)^{34}$ for each sample, as shown in Fig. S4(d).† It can be found from Fig. 10(b) that the lattice thermal conductivity of pure PbTe alloy first decreases, reaches a plateau and then slightly decreases with increase in temperature in the whole measured temperature range. The plateau of lattice thermal conductivity may result from the combined effects of p–n transition and bipolar thermal conductivity. As previously reported, lattice thermal conductivity often changes suddenly at phase transition regions.^{35,36} In addition, the bipolar thermal conductivity always exists, which is reported in previous studies.^{28,31,32} Thus, these two factors and their combined effects may cause this plateau in a certain temperature range. With Bi doping, p–n transition and bipolar effect are removed and prohibited. Thus, the lattice thermal conductivities continue to decrease with increase in temperature over the transition temperature range of the pristine sample. Lattice thermal conductivity of $0.68 \text{ W m}^{-1} \text{K}^{-1}$ is achieved at 673 K. Additionally, the lattice thermal conductivities do not show clear changes with various amounts of Bi; this is in accordance with the results of Bi-doped PbTe alloys synthesized by the conventional melting method.²¹ However, lattice thermal conductivities decrease significantly at middle and high temperature ranges with Bi doping compared with that of pristine PbTe alloy. As described above, the bipolar effect is prohibited in Bi-doped alloys, which may be the main factor to reduce the lattice thermal conductivity at middle and high temperature ranges in these samples. Besides the prohibition of bipolar thermal conductivity, the scattering of alloys, grain boundaries, dislocations and defects are also introduced and strengthened by Bi doping on Pb sites. The reduction in lattice thermal conductivity is also ascribed to these factors. In the end, the lowest lattice thermal conductivity of $0.68 \text{ W m}^{-1} \text{K}^{-1}$ is obtained for $\text{Pb}_{0.98}\text{Bi}_{0.02}$ alloy at 673 K, and its total thermal conductivity of $0.85 \text{ W m}^{-1} \text{K}^{-1}$ is also the lowest when compared with the values of all samples.

The figures of merits, zT s, of $\text{Pb}_{1-x}\text{Bi}_x\text{Te}$ alloys are shown in Fig. 11(a). The figures of merit of all Bi-doped PbTe samples increase with increasing temperature within the measured temperature limit. This is due to the shift of peak power factors to a high temperature range and significant reduction in thermal conductivity at a high temperature, as described above. Thus, peak values of figures of merit are obtained at 673 K for all Bi-doped PbTe samples. The highest peak figure of merit $zT = 0.62$ is achieved for $\text{Pb}_{0.98}\text{Bi}_{0.02}\text{Te}$ alloy, which is enhanced by about 9 times compared with that of pristine PbTe alloy at 673 K. The average figure of merit is calculated based on eqn (1):

$$zT_{\text{ave}} = \frac{1}{T_h - T_c} \int_{T_c}^{T_h} zT dT \quad (1)$$

here, T_h and T_c are the hot-side and cold-side temperatures, respectively. The average figures of merit values for all samples are shown in Fig. 11(b). All average figures of merit values, zT_{ave} , are in the range of 0.25–0.3 at the temperature range of 323–673 K for Bi-doped samples, whereas zT_{ave} is only near 0.1

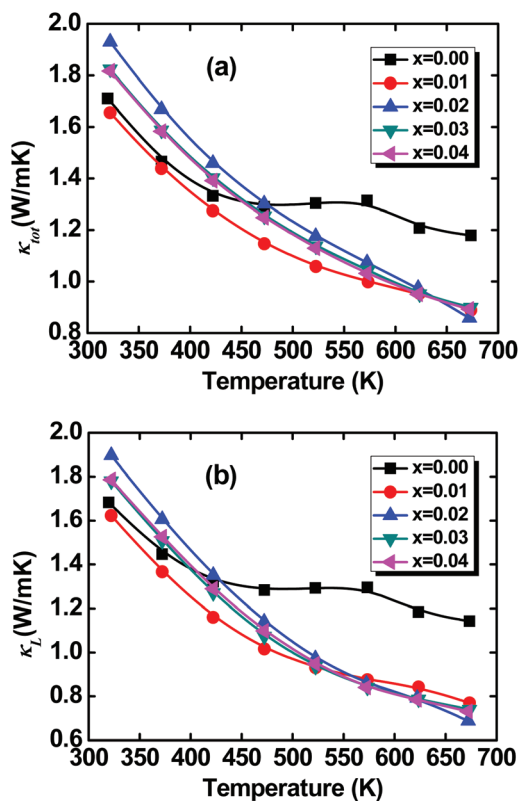


Fig. 10 The temperature dependence of (a) total thermal conductivity and (b) lattice thermal conductivity for $\text{Pb}_{1-x}\text{Bi}_x\text{Te}$ alloys.

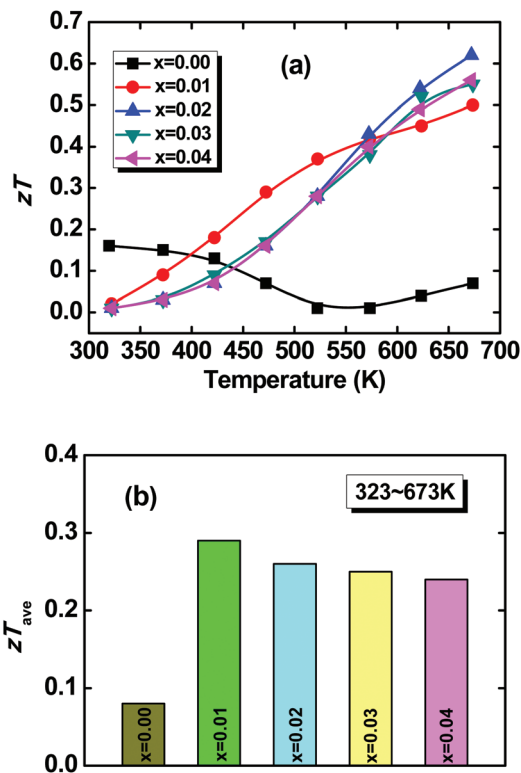


Fig. 11 (a) The temperature dependence of the figure of merit and (b) average figure of merit for $\text{Pb}_{1-x}\text{Bi}_x\text{Te}$ alloys at 323–673 K.

for pristine PbTe alloy. This is because the figures of merit at the middle and high temperature ranges are enhanced by Bi doping, as shown in Fig. 11(a). $\text{Pb}_{0.99}\text{Bi}_{0.01}\text{Te}$ alloy shows the highest average figure of merit (zT_{ave} , ~ 0.3), which is improved by about 3 times compared with that of pure PbTe alloy. This mainly results from the highest figure of merit at low and middle temperature ranges.

Fig. 12(a) presents comparisons of figures of merit at 673 K for $\text{Pb}_{1-x}\text{Bi}_x\text{Te}$ alloys with different synthesis methods. The figures of merit of Bi-doped samples synthesized by the microwave hydrothermal method are comparable with reported values for samples prepared by conventional melting methods. The maximum figure of merit achieved in this study is $zT = 0.62$, whereas the reported zT value is about 0.7 at the same temperature point. In addition to figure of merit, synthesis time and temperature are also compared herein. For the microwave hydrothermal method followed by hot pressing conducted in this study, the total synthesis time is about 2 hours, as described in the Experimental section. The reported melting synthesis and SPS method has a preparation time of about 40 hours. It is clearly seen that the microwave hydrothermal method followed by hot pressing can rapidly result in $\text{Pb}_{1-x}\text{Bi}_x\text{Te}$ alloys with comparable figures of merit. In addition, the synthesis temperature of microwave hydrothermal method is generally low: it is only 140 °C for $\text{Pb}_{1-x}\text{Bi}_x\text{Te}$ samples. Although $\text{Pb}_{1-x}\text{Bi}_x\text{Te}$ alloys have comparable thermoelectric figures of merit when synthesized by these

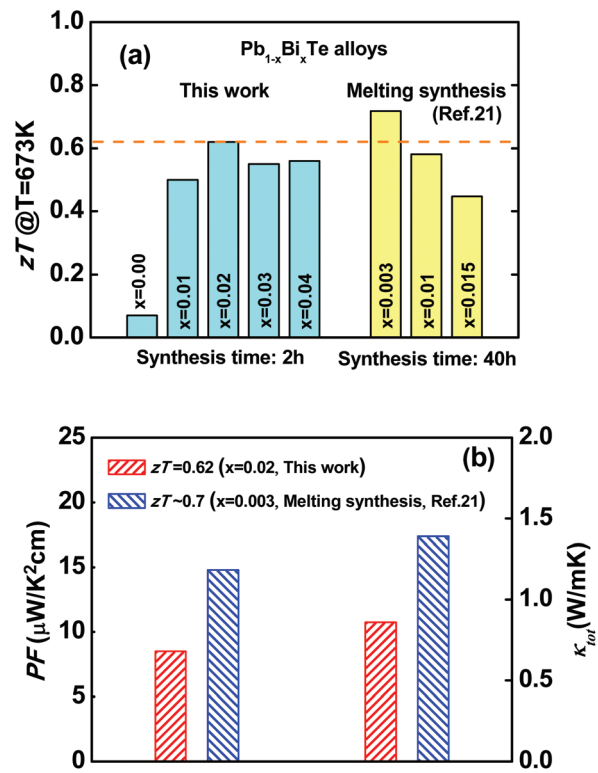


Fig. 12 (a) Comparison of figures of merit for $\text{Pb}_{1-x}\text{Bi}_x\text{Te}$ alloys with different synthesis methods. (b) Power factor and total lattice thermal conductivity for $\text{Pb}_{1-x}\text{Bi}_x\text{Te}$ composition with the highest zT value synthesized with different methods.

two methods, the main influencing factors on thermoelectric parameters are different, as shown in Fig. 12(b). The power factor obtained in this study is much inferior, but thermal conductivity is significantly lower. This may be related to the fine grains formed by the microwave hydrothermal method. Thus, the comparable figure of merit obtained by the microwave hydrothermal method is mostly due to low thermal conductivity or optimized microstructure. By comprehensively analysing the effect of microwave hydrothermal synthesis on the thermoelectric performance of n-type $\text{Pb}_{1-x}\text{Bi}_x\text{Te}$ alloys, it can be concluded that this synthesis method at right reaction conditions may be much better for optimizing this kind of thermoelectric material, which has high electrical properties and thermal conductivity.

Conclusions

N-type $\text{Pb}_{1-x}\text{Bi}_x\text{Te}$ alloys with $x = 0.00, 0.01, 0.02, 0.03$ and 0.04 have been rapidly synthesized by the microwave hydrothermal method followed by hot pressing. Single cubic crystal structures, compact microstructures and homogenous element distribution have been formed in all samples. The solid solubility limit of Bi in PbTe has been confirmed to be between $x = 0.02$ and 0.03 . Most grain sizes of Bi-doped samples are at sub-microscale and are smaller than those of pristine PbTe.

With increase in Bi content, the carrier concentration is improved until the solubility limit, and the lowest electrical resistivity is found at $x = 0.02$ and 0.03 . The values of Seebeck coefficients are negative with Bi doping, and the change in behavior with Bi content is consistent with carrier concentration. Following that, the maximum power factor value of about $8.5 \mu\text{W cm}^{-1} \text{K}^{-2}$ has been achieved at 623 K for $x = 0.02$. Since bipolar thermal conductivity is prohibited with the introduction of Bi, the lattice thermal conductivity is still low with increase in temperature. In addition, the scattering of alloys, grain boundaries, dislocations, and defects are introduced and strengthened. Thus, the lowest lattice thermal conductivity of $0.68 \text{ W m}^{-1} \text{K}^{-1}$ is obtained at 673 K for $\text{Pb}_{0.98}\text{Bi}_{0.02}\text{Te}$ alloy. As a result, the improved power factor at high temperature and lowest lattice thermal conductivity lead to the highest figure of merit of $zT = 0.62$ at 673 K for $\text{Pb}_{0.98}\text{Bi}_{0.02}\text{Te}$. This figure of merit is comparable to that of Bi-doped PbTe alloys synthesized by the conventional melting method. Therefore, the microwave hydrothermal method at optimized reaction conditions can rapidly result in n-type $\text{Pb}_{1-x}\text{Bi}_x\text{Te}$ alloys with comparable thermoelectric performance.

Conflicts of interest

There are no conflicts to declare.

Acknowledgements

The work is financially supported by the National Basic Research Program of China of 2013CB632506, the Natural Science Fund of China under grant No. 51501105, 51672159, 51871134, 51611540342, the Young Scholars Program of Shandong University under grant No. 2015WLJH21, the China Postdoctoral Science Foundation under grant No. 2015M580588 and 2016T90631, the Postdoctoral Innovation Foundation of Shandong Province under grant No. 201603027, and the Foundation of the State Key Laboratory of Metastable Materials Science and Technology under grant No. 201703.

Notes and references

- 1 Y. Z. Pei, X. Shi, A. LaLonde, H. Wang, L. D. Chen and G. J. Snyder, *Nature*, 2011, **473**, 66–69.
- 2 T. Z. Zhu, Y. T. Liu, C. G. Fu, J. P. Heremans, J. G. Snyder and X. B. Zhao, *Adv. Mater.*, 2017, **29**, 1605884.
- 3 L. D. Zhao, G. G. Tan, S. Q. Hao, J. Q. He, Y. L. Pei, H. Chi, H. Wang, S. K. Gong, H. B. Xu, V. P. Dravid, C. Uher, G. J. Snyder, C. Wolverton and M. G. Kanatzidis, *Science*, 2016, **351**, 141–144.
- 4 W. Y. Zhao, Z. Y. Liu, Z. G. Sun, Q. J. Zhang, P. Wei, X. Mu, H. Y. Zhou, C. C. Li, F. S. Ma, D. Q. He, P. X. Ji, W. T. Zhu, X. L. Nie, X. L. Su, X. F. Tang, B. G. Shen, X. L. Dong, J. H. Yang, Y. Liu and J. Shi, *Nature*, 2017, **549**, 247–251.
- 5 C. Chang, M. H. Wu, D. S. He, Y. L. Pei, C. F. Wu, X. F. Wu, H. L. Yu, F. Y. Zhu, K. D. Wang, Y. Chen, L. Huang, J. F. Li, J. Q. He and L. D. Zhao, *Science*, 2018, **360**, 778–783.
- 6 H. C. Wang, J. Hwang, C. Zhang, T. Wang, W. B. Su, H. Kim, J. Kim, J. Z. Zhai, X. Wang, H. Park, W. Kim and C. L. Wang, *J. Mater. Chem. A*, 2017, **5**, 14165–14173.
- 7 Y. Z. Pei, Z. M. Gibbs, A. Gloskovskii, B. Balke, W. G. Zeier and G. J. Snyder, *Adv. Energy Mater.*, 2014, **4**, 1400486.
- 8 Q. Zhang, F. Cao, W. S. Liu, K. Lukas, B. Yu, S. Chen, C. Opeil, D. Broido, G. Chen and Z. F. Ren, *J. Am. Chem. Soc.*, 2012, **134**, 10031–10038.
- 9 A. D. LaLonde, Y. Z. Pei and G. J. Snyder, *Energy Environ. Sci.*, 2011, **4**, 2090–2096.
- 10 H. Wang, J. H. Bahk, C. Kang, J. Hwang, K. Kim, A. Shakouri and W. Kim, *J. Mater. Chem. A*, 2013, **1**, 11269–11278.
- 11 K. Biswas, J. Q. He, I. D. Blum, C. I. Wu, T. P. Hogan, D. N. Seidman, V. P. Dravid and M. G. Kanatzidis, *Nature*, 2012, **489**, 414–418.
- 12 W. Kim, J. Zide, A. Gossard, D. Klenov, S. Stemmer, A. Shakouri and A. Majumdar, *Phys. Rev. Lett.*, 2006, **96**, 045901.
- 13 H. C. Wang, J. Hwang, M. L. Snedaker, I. H. Kim, C. Kang, J. Kim, G. D. Stucky, J. Bowers and W. Kim, *Chem. Mater.*, 2015, **27**, 944–949.
- 14 H. J. Wu, L. D. Zhao, F. S. Zheng, D. Wu, Y. L. Pei, X. Tong, M. G. Kanatzidis and J. Q. He, *Nat. Commun.*, 2014, **5**, 4515.
- 15 D. Wu, L. D. Zhao, X. Tong, W. Li, L. J. Wu, Q. Tan, Y. L. Pei, L. Huang, J. F. Li, Y. M. Zhu, M. G. Kanatzidis and J. Q. He, *Energy Environ. Sci.*, 2015, **8**, 2056–2068.
- 16 H. C. Wang, J. H. Bahk, C. Kang, J. Hwang, K. Kim, J. Kim, P. Burke, J. E. Bowers, A. C. Gossard, A. Shakouri and W. Kim, *Proc. Natl. Acad. Sci. U. S. A.*, 2014, **111**, 10949–10954.
- 17 Y. L. Pei, G. J. Tan, D. Feng, L. Zheng, Q. Tan, X. B. Xie, S. K. Gong, Y. Chen, J. F. Li, J. Q. He, M. G. Kanatzidis and L. D. Zhao, *Adv. Energy Mater.*, 2017, **7**, 1601450.
- 18 G. J. Tan, F. Y. Shi, S. Q. Hao, L. D. Zhao, H. Chi, X. M. Zhang, C. Uher, C. Wolverton, V. P. Dravid and M. G. Kanatzidis, *Nat. Commun.*, 2016, **7**, 12167.
- 19 Z. W. Chen, Z. Z. Jian, W. Li, Y. J. Chang, B. H. Ge, R. Hanus, J. Yang, Y. Chen, M. Huang, G. J. Snyder and Y. Z. Pei, *Adv. Mater.*, 2017, **29**, 1606768.
- 20 Y. Z. Pei, J. Lensch-Falk, E. S. Toberer, D. L. Medlin and G. J. Snyder, *Adv. Funct. Mater.*, 2011, **21**, 241–249.
- 21 G. J. Tan, C. C. Stoumpos, S. Wang, T. P. Bailey, L. D. Zhao, C. Uher and M. G. Kanatzidis, *Adv. Energy Mater.*, 2017, **7**, 1700099.
- 22 J. Zhang, D. Wu, D. S. He, D. Feng, M. J. Yin, X. U. Qin and J. Q. He, *Adv. Mater.*, 2017, **29**, 1703148.
- 23 L. W. Fu, M. J. Yin, D. Wu, W. Li, D. Feng, L. Huang and J. Q. He, *Energy Environ. Sci.*, 2017, **10**, 2030–2040.
- 24 R. J. Mehta, Y. L. Zhang, C. Karthik, B. Singh, R. W. Siegel, T. Borca-Tasciuc and G. Ramanath, *Nat. Mater.*, 2012, **11**, 233–240.

- 25 Z. L. Li, Y. D. Chen, J. F. Li, H. Chen, L. J. Wang, S. Q. Zheng and G. W. Lu, *Nano Energy*, 2016, **28**, 78–86.
- 26 Y. Li, C. Cheng, Y. Lei, M. Wang and R. D. Wan, *Dalton Trans.*, 2016, **46**, 33–38.
- 27 R. Blachnik and R. Igel, *Z. Naturforsch., B: J. Chem. Sci.*, 1974, **29**, 625–629.
- 28 F. R. Sie, H. J. Liu, C. H. Kuo, C. S. Hwang, Y. W. Chou and C. H. Yeh, *Intermetallics*, 2018, **92**, 113–118.
- 29 E. J. Menke, M. A. Brown, Q. Li, J. C. Hemminger and R. M. Penner, *Langmuir*, 2006, **22**, 10564–10574.
- 30 Q. Zhang, T. Sun, F. Cao, M. Li, M. H. Hong, J. K. Yuan, Q. Yan, H. H. Hng, N. Q. Wu and X. G. Liu, *Nanoscale*, 2010, **2**, 1256–1259.
- 31 A. Schmitz, C. Stiewe, K. Zabrocki, J. de Boor, K. Mull and E. Müller, *Mater. Res. Bull.*, 2017, **86**, 159–166.
- 32 G. C. Ding, J. X. Si, H. F. Wu, S. D. Yang, J. Zhao and G. W. Wang, *J. Alloys Compd.*, 2016, **662**, 368–373.
- 33 H. C. Wang, C. L. Wang, W. B. Su, J. Liu, Y. Zhao, H. Peng, J. L. Zhang, M. L. Zhao, J. C. Li, N. Yin and L. M. Mei, *Mater. Res. Bull.*, 2010, **45**, 809–812.
- 34 H. S. Kim, Z. M. Gibbs, Y. Tang, H. Wang and G. J. Snyder, *APL Mater.*, 2015, **3**, 041506.
- 35 H. L. Liu, X. Yuan, P. Lu, X. Shi, F. F. Xu, Y. He, Y. S. Tang, S. Q. Bai, W. Q. Zhang, L. D. Chen, Y. Lin, L. Shi, H. Lin, X. Y. Gao, X. M. Zhang, H. Chi and C. Uher, *Adv. Mater.*, 2013, **25**, 6607–6612.
- 36 C. Xiao, X. M. Qin, J. Zhang, R. An, J. Xu, K. Li, B. X. Cao, J. L. Yang, B. J. Ye and Y. Xie, *J. Am. Chem. Soc.*, 2012, **134**, 18460–18466.